An atlas of carbon nanotube optical transitions

Kaihui Liu[1,2], Jack Deslippe[1,3], Fajun Xiao[1,4], Rodrigo B. Capaz[1,5], Xiaoping Hong[1], Shaul Aloni[6], Alex Zettl[1,3], Wenlong Wang[2], Xuedong Bai[2], Steven G. Louie[1,3], Enge Wang[7]* and Feng Wang[1,3]*

Electron–electron interactions are significantly enhanced in one-dimensional systems[1], and single-walled carbon nanotubes provide a unique opportunity for studying such interactions and the related many-body effects in one dimension[2-4]. However, single-walled nanotubes can have a wide range of diameters and hundreds of different structures, each defined by its chiral index (n,m)[5,6], where n and m are integers that can have values from zero up to 30 or more. Moreover, one-third of these structures are metals and two-thirds are semiconductors, and they display optical resonances at many different frequencies. Systematic studies of many-body effects in nanotubes would therefore benefit from the availability of a technique for identifying the chiral index of a nanotube based on a measurement of its optical resonances, and vice versa. Here, we report the establishment of a structure–property 'atlas' for nanotube optical transitions based on simultaneous electron diffraction measurements of the chiral index and Rayleigh scattering measurements of the optical resonances[7,8] of 206 different single-walled nanotube structures. The nanotubes, which were suspended across open slit structures on silicon substrates, had diameters in the range 1.3–4.7 nm. We also use this atlas as a starting point for a systematic study of many-body effects in the excited states of single-walled nanotubes[9-16]. We find that electron–electron interactions shift the optical resonance energies by the same amount for both metallic and semiconducting nanotubes, and that this shift (which corresponds to an effective Fermi velocity renormalization) increases monotonically with nanotube diameter. This behaviour arises from two sources: an intriguing cancellation of long-range electron–electron interaction effects, and the dependence of short-range electron–electron interactions on diameter[10,11].

The results for three representative single-walled carbon nanotubes are shown in Fig. 1. From the electron diffraction pattern for the first of these nanotubes (Fig. 1a) we determine its chiral index to be (18,7), which means that this is a semiconducting nanotube with a diameter of 1.75 nm. The second nanotube (Fig. 1b) has a chiral index of (30,22), which means that it is also semiconducting (with a diameter of 3.54 nm). The third nanotube (Fig. 1c) has a chiral index of (24,24), which means that it is metallic with a diameter of 3.25 nm. Each nanotube also exhibits distinct optical resonances in its Rayleigh spectrum (Fig. 1d–f). Our data complement previous fluorescence studies of nanotubes with diameters in the range 0.6–1.3 nm (refs 17,18), and together they can be used as an atlas for determining the chiral index of a single-walled nanotube from a measurement of its optical resonances, and vice versa (Supplementary Section S4).

A number of techniques can be used to determine the chiral index and optical resonances of single-walled nanotubes (hereafter called nanotubes), but they are all limited in various ways. Fluorescence excitation spectroscopy, for example, allows the chiral index to be determined from measurements of the fluorescence, but only for a small subset of semiconducting nanotubes[17]. Raman spectroscopy is a more general technique, in principle, but it suffers from large uncertainties due to the presence of many overlapping resonant peaks from ensemble measurements[19-21]. The uncertainty in our determination of the optical resonances for all nanotubes is less than 20 meV. This is significantly more accurate than previous comprehensive optical assignments based on Raman mapping, where the difference between the measured and predicted optical transition energies is greater than 100 meV for many nanotubes[21].

It should be noted that our results are based on suspended nanotubes. It is known that environmental effects, such as the presence of a substrate or surrounding micelles, can redshift the optical transition, predominantly due to dielectric screening. A comparison of nanotubes suspended in air and nanotubes embedded in micelles shows that this redshift is relatively constant at ∼20 meV for different nanotubes[18], and similar redshifts are expected for nanotubes deposited on substrates. Accordingly, a suitable correction should be made when characterizing nanotubes that are not suspended in air.

The relationship between the chiral index and the optical resonances of nanotubes reported here allows for a systematic examination of excited-state properties in one-dimensional nanotubes. Although the optical transitions in nanotubes are excitonic in nature, a convenient scheme by which to categorize the optical transitions in an (n,m) nanotube is the zone-folding technique, in which the periodic boundary condition around the nanotube circumference leads to a quantization of wave vector (**k**), described by parallel lines separated by $2/d$ in the graphene Brillouin zone[5,6]. In metallic nanotubes, one of the parallel **k**-lines passes through the K-point, which occurs when mod$(n-m,3) = 0$ (Fig. 2a). The other nanotubes are semiconducting with mod$(n-m,3) = 1$ or 2 (Fig. 2b). Each parallel **k**-line describes one pair of conduction and valence sub-bands in the nanotube. Transitions at the bandgaps of such sub-band pairs lead to strong optical resonances, and these transitions are traditionally labelled S_{ii} for semiconducting and M_{ii} for metallic nanotubes, where i is the sub-band index. Equivalently, we can introduce an integer p $(= 1,2,3,4,5,6, \ldots)$ to index optical transitions in both semiconducting and metallic nanotubes in the order of S_{11}, S_{22}, M_{11}, S_{33}, S_{44}, M_{22}, S_{55}, S_{66}, M_{33}, S_{77}, ... (Table 1). Each nanotube optical transition can be associated with a specific wave vector $\mathbf{k}_p^{(n,m)}$ (for example, red dots in Fig. 2a,b) in the graphene Brillouin zone that varies with nanotube chirality (n,m) and transition index p (for a detailed relation see Supplementary Section S2). The magnitude of $\mathbf{k}_p^{(n,m)}$ has a value of $p \times 2/(3d)$.

The one-to-one mapping between a nanotube optical resonance and a wave vector in the graphene Brillouin zone provides a

[1]Department of Physics, University of California at Berkeley, Berkeley, California 94720, USA, [2]Institute of Physics, Chinese Academy of Sciences, Beijing 100190, China, [3]Materials Science Division, Lawrence Berkeley National Laboratory, Berkeley, California 94720, USA, [4]School of Science, Northwestern Polytechnic University, Xi'an 710072, China, [5]Instituto de Física, Universidade Federal do Rio de Janeiro, Caixa Postal 68528, Rio de Janeiro, RJ 21941-972, Brazil, [6]The Molecular Foundry, Lawrence Berkeley National Laboratory, Berkeley, California 94720, USA, [7]International Center for Quantum Materials, School of Physics, Peking University, Beijing 100871, China. *e-mail: fengwang76@berkeley.edu; egwang@pku.edu.cn
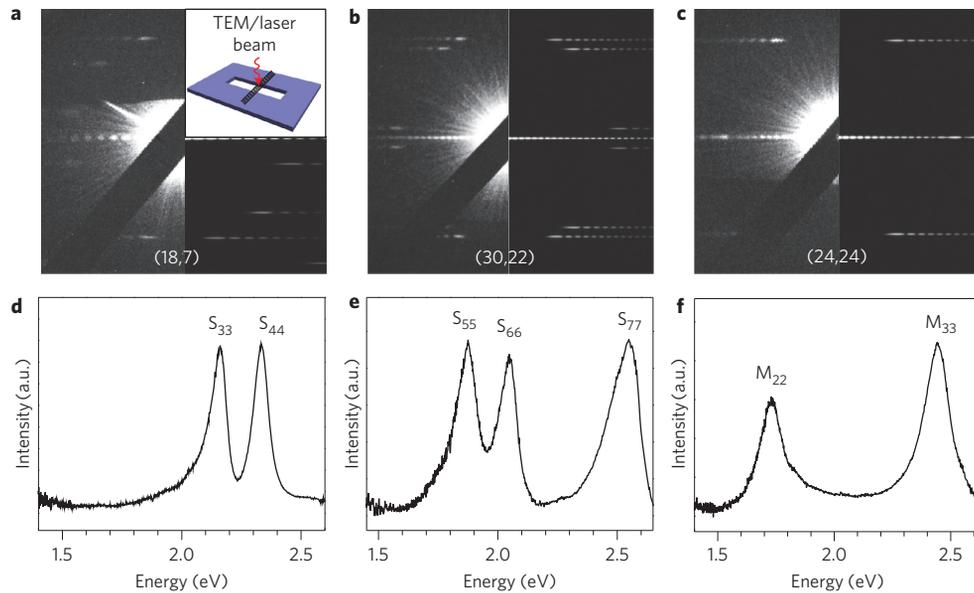
Figure 1 | Electron diffraction patterns and Rayleigh spectra of three representative nanotubes. a–c, Electron diffraction patterns (left, experimental; right, simulated) for three single-walled nanotubes with different chiral indices. The zero-order and high-order diffraction bands uniquely define the chiral index (n,m) of the nanotube. The (18,7) nanotube (**a**) is semiconducting and has a diameter of 1.75 nm. Inset: schematic for combined TEM electron diffraction and Rayleigh scattering measurements on the same suspended nanotube. The black diagonal feature is caused by the blocking stick used for dark-field imaging. The (30,22) nanotube (**b**) is semiconducting and has a diameter of 3.54 nm. The (24,24) nanotube (**c**) is metallic and has a diameter of 3.25 nm. **d–f,** Rayleigh spectra for the three nanotubes in **a–c**.
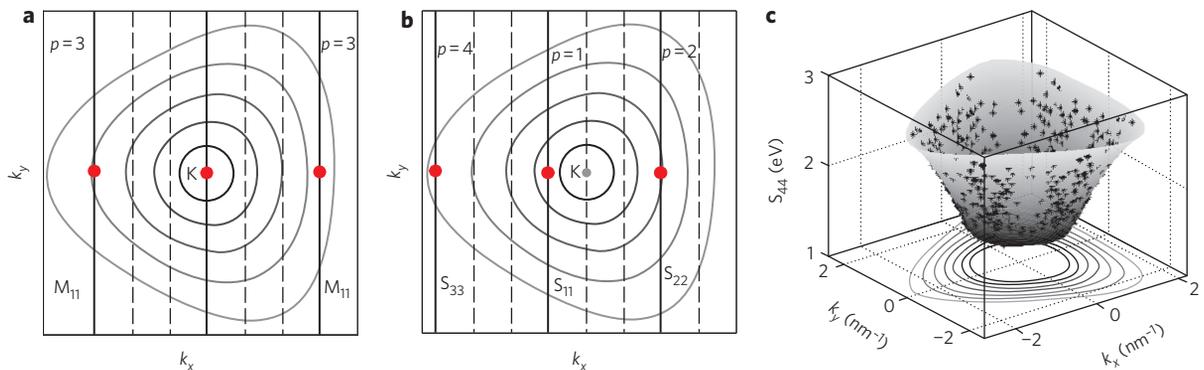
Figure 2 | Momentum-resolved transitions with nanotube optical resonances. a,b, Zone-folding pictures of metallic (**a**) and semiconducting (**b**) nanotubes. The contour curves are constant energy lines in the graphene Brillouin zone. The solid parallel lines describe available states consistent with the nanotube boundary condition, which are separated by $2/d$ in the graphene Brillouin zone. (The dashed parallel lines are a guide to the eye with a separation of $2/(3d)$.) The solid lines can be indexed by an integer p describing their distance from the K-point as $p \times 2/(3d)$, and each solid parallel line corresponds to a pair of conduction and valence sub-bands in the nanotubes. Metallic nanotubes have p values of $0,3,6,\ldots$ and semiconducting nanotubes have p values of $1,2,4,5,\ldots$ Nanotube optical resonance, arising from the bandgap of a sub-band pair, is associated with a specific wave vector $\mathbf{k}_p^{(n,m)}$ (red dots in **a** and **b**) in the graphene Brillouin zone. For a given p, different nanotubes (with different n and m) have optical transition energies E_p corresponding to different $\mathbf{k}$-points, and this E_p–$\mathbf{k}$ relation defines an effective dispersion relation $E_p(\mathbf{k})$. **c,** Momentum-resolved transition energy dispersion $E_p(\mathbf{k})$ for $p=5$ (corresponding to the S_{44} transition). Each nanotube samples out a certain E_p–$\mathbf{k}$ dot in the graphene Brillouin zone, and the collection of such an E_p–$\mathbf{k}$ correspondence from different nanotubes defines an effective dispersion relation $E_p(\mathbf{k})$ for transition $p=5$. Dots are experimental data, and the surface plot is based on empirical equation (1).

framework to describe the chirality dependence of nanotube optical transitions. For the pth transition in each given nanotube (with indices n and m), its transition energy (E_p) and underlying wave vector ($\mathbf{k}_p^{(n,m)}$) establishes one E_p–$\mathbf{k}$ correspondence. A collection of such E_p–$\mathbf{k}$ correspondences from different nanotubes, which sample different $\mathbf{k}$-points in the graphene Brillouin zone, defines an effective dispersion relation $E_p(\mathbf{k})$ for transition p. Figure 2c displays such a 'momentum-resolved' transition energy dispersion for $p=5$ (S_{44}). If we neglect possible one-dimensional effects arising in nanotubes, $E_p(\mathbf{k})$ of nanotubes will reproduce exactly the inter-band

optical transition dispersion in two-dimensional graphene and p will be a redundant index. Any p-dependence of $E_p(\mathbf{k})$ (that is, a deviation of $E_p(\mathbf{k})$ from the corresponding dispersion in suspended graphene) therefore probes changes in the many-body interaction effects and curvature effects specific to one-dimensional nanotubes. Also, because p is proportional to nanotube diameter (for fixed k with $p=1.5kd$) and it indexes all nanotube types, the evolution of $E_p(\mathbf{k})$ with p will shed light on how many-body effects differ in metallic and semiconducting nanotubes and how they evolve with nanotube diameter towards the suspended two-dimensional graphene limit.

Table 1 | Integer p and fitting parameters v_F, η and β of empirical equation (1) (described in the text for different optical transitions).

Transition	p	v_F (10^6 m s^{-1})	η (eV nm^2)	β (eV nm^2)
S$_{11}$	1	1.229	0.142	−0.173
S$_{22}$	2	1.152	0.097	
M$_{11}$	3	1.176	0.068	
S$_{33}$	4	1.221	0.058	
S$_{44}$	5	1.226	0.058	
M$_{22}$	6	1.236	0.058	
S$_{55}$	7	1.241	0.047	
S$_{66}$	8	1.244	0.052	
M$_{33}$	9	1.248	0.047	
S$_{77}$	10	1.256	0.054	

S$_{11}$ and S$_{22}$ data are from ref. 17 with slightly shifted energy (20 meV for S$_{11}$ and 15 meV for S$_{22}$) to compensate for the micelle-induced redshifts[18]. To obtain the resonance energy for a specific optical transition in an (n,m) nanotube, one can plug the listed parameters into equation (1) and use (k, θ) values obtained from zone folding.

To describe the effective dispersion such as that in Fig. 2c, we introduce an empirical formula

$$E_p(\mathbf{k}) = 2\hbar v_F(p) \times k + \beta \times k^2 + \eta(p) \times k^2 \cos(3\theta) \quad (1)$$

Here, k and θ are polar coordinates for the magnitude and direction of wave vector $\mathbf{k}$. The dominating first term characterizes the linear Dirac cone in the graphene band structure with an effective Fermi velocity $v_F(p)$. The second and third terms describe, respectively, deviation from the linear dispersion away from the Dirac point and deviation from a circular cone due to the graphene trigonal symmetry. The p-dependent effective Fermi velocity $v_F(p)$ and anisotropy prefactor $\eta(p)$ are included to account for nanotube-specific physics. Using this formula we were able to fit all 522 transitions from 206 individual nanotubes in our study with an overall uncertainty of less than 20 meV. Table 1 summarizes the values of $v_F(p)$, β and $\eta(p)$ in equation (1) that were used to fit our data, as well as those obtained from fluorescence excitation spectroscopy[17,18]. Figure 3a shows the k-region covered by experimentally observed optical transitions for $p = 1$ to 10.

We first examine the renormalization of $v_F(p)$, which characterizes the angle-independent change in the slope of the E_p–$\mathbf{k}$ dispersion. This angle-independent component can be conveniently obtained by slicing the full E_p–$\mathbf{k}$ dispersion (Fig. 2c) along the armchair direction (that is, with $\theta = 30°$ and $210°$ in equation (1)). Figure 3b displays the results for $p = 2$ (orange curve) and $p = 9$ (blue curve). They are symmetric over the K-point ($k = 0$), but exhibit a clearly different slope, or effective v_F. The overall dependence of $v_F(p)$ on p (or equivalently on $\bar{d}$ on the top axis) is shown in Fig. 3c. It shows a renormalization of the 'effective Fermi velocity' (v_F) in nanotubes. This renormalization arises from many-body effects due to electron–electron interactions, and it varies between different nanotube species.

The magnitude of renormalization in the Fermi velocity depends on both the nanotube diameter and the k-vector region in the graphene Brillouin zone. Because experimental data for transition $p = 1$ (S$_{11}$) have k values much smaller than other transitions (Fig. 3a), its comparison to other transitions requires that the k-dependent renormalization effects be taken into account. Qualitatively, we can attribute the observed relatively large effective Fermi velocity for $p = 1$ transitions to this k-dependence, but a quantitative theoretical description of the k-dependence of the renormalization is beyond our experimental work. Transitions $p = 2$ to 10, however, cover largely the same overlapped k-region (Fig. 3a). They provide a unique opportunity for us to isolate the diameter dependence of the renormalization of the Fermi velocity, which can be described by $v_F(p) = (1.277 - 0.267/p) \times 10^6$ m s^{-1} (solid line of Fig. 3c). It shows two surprising behaviours: (i) a higher effective v_F, which is associated with enhanced electron–electron interactions[9–12], is observed in larger-diameter nanotubes; and (ii) v_F values for semiconducting and metallic nanotube transitions fall on exactly the same curve. These experimental observations provide a striking demonstration of the different effects of the long-range and short-range components of electron–electron interactions in excited states of one-dimensional nanotubes, first described theoretically in the pioneering work of Kane and Mele[10,11].

It has been shown theoretically that the long-range interactions have cancelling effects on bandgap renormalization and exciton formation[9–16]. In particular, ref. 11 provides a rigorous argument that

Figure 3 | Renormalization of the effective Fermi velocity and its p-dependence. a, Wave-vector range in the graphene Brillouin zone where experimental data exist for different transitions. The k-values for the $p = 1$ transition are much smaller than those for other transitions. For transitions $p = 2$ to 10, the experimental data overlap well in the range $1.2 < k < 1.8$ nm^{-1} (between dashed lines). In this selected k-region, p values from 2 to 10 correspond to average nanotube diameters ($\bar{d}$) from 0.9 to 4.4 nm, and they include three metallic ($p = 3,6,9$) and six semiconducting resonances ($p = 2,4,5,7,8,10$). **b**, $E_p(\mathbf{k})$ dispersion along the armchair direction (that is, with $\theta = 30°$ and $210°$) for transitions $p = 2$ (orange line) and $p = 9$ (blue line). These characterize the angle-independent component of transition energy dispersion. Dispersion for $p = 9$ shows a significantly increased slope (that is, effective v_F). **c**, Renormalized effective Fermi velocity v_F as a function of p. For transitions of $p = 2$ to 10 covering the same k-region, p is proportional to $\bar{d}$ in the top axis, and the diameter-dependent renormalization is well described by $v_F(p) = (1.277 - 0.267/p) \times 10^6$ m s^{-1} (solid line). Surprisingly, this reveals that v_F values for semiconducting and metallic nanotube transitions fall on exactly the same curve, despite their dramatically different electron–electron interactions. On the other hand, electron–electron interaction induced v_F renormalization increases systematically with nanotube diameter. The effective Fermi velocity for the $p = 1$ transition does not follow the common trend because this transition has k-values much smaller than other transitions (**a**). Its v_F is relatively large due to the k-dependence of renormalization, in contrast to the diameter-dependent behaviour for transitions $p = 2$ to 10.
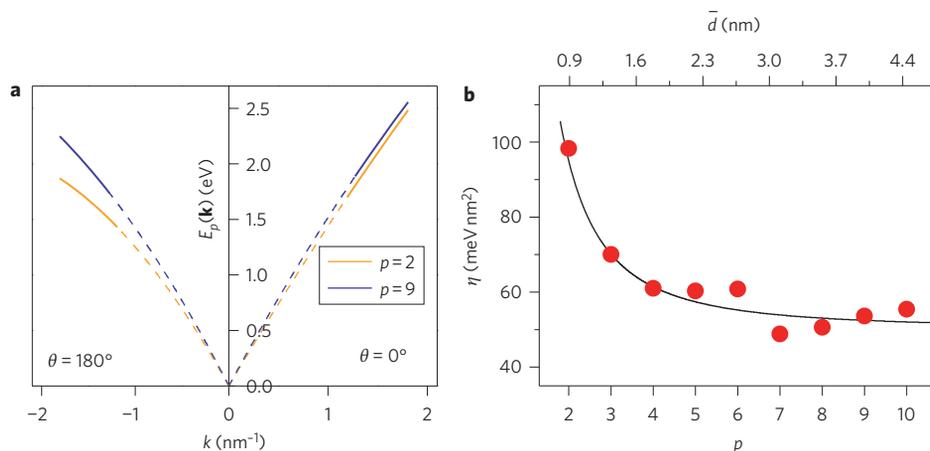
Figure 4 | Trigonal asymmetry. a, $E_p(\mathbf{k})$ dispersion along the zigzag direction (that is, with $\theta = 0°$ and $180°$) for transitions $p = 2$ (orange line) and $p = 9$ (blue line). The trigonal anisotropy of the dispersion is obvious from the asymmetry between the $\theta = 0°$ and $180°$ directions (corresponding to positive and negative k-values, respectively), and the asymmetry is markedly stronger for the transition $p = 2$. **b**, Anisotropy prefactor $\eta(p)$ for different p (or equivalently on $\bar{d}$ in the top axis). It is well described by the expression $\eta(p) = (50 + 180/p^2)$ meV nm^2 (solid line). This diameter dependence of trigonal anisotropy arises from strain effects and σ–π bond hybridization due to the finite nanotube curvature.

the cancellation is perfect for a constant long-range interaction. Here, we demonstrate experimentally that such cancellation is almost perfect for the actual long-range interaction in nanotubes: the semiconducting and metallic nanotubes have drastically different long-range electron–electron interactions, but their optical transition energies fall perfectly on the same curve (Fig. 3c).

Short-range electron–electron interactions, however, show qualitatively different behaviour: they produce a significant net blueshift of optical transition energies[9–11]. Reference 11 shows theoretically that the effect of short-range interactions increases slightly but systematically with nanotube diameter, in contrast to the common notion that many-body effects are always stronger in more one-dimensional structures. We demonstrate this diameter dependence of short-range interaction experimentally in that $v_F(p)$ (that is, optical transition energy at the same $\mathbf{k}$) increases with nanotube diameter. Interestingly, the effective Fermi velocity in large-diameter nanotubes should approach the 'intrinsic' v_F in suspended graphene, and our measurements suggest a value of 1.28×10^6 m s^{-1}. This is significantly larger than most reported Fermi velocity values for supported graphene[22,23], presumably due to reduced electron–electron interactions and Fermi velocity renormalization from substrate screening in supported samples.

Finally, we examine the p-dependent $\eta(p)$, which describes the changes in trigonal anisotropy in the energy dispersion. This is best illustrated by slicing the full $E_p(\mathbf{k})$ dispersion (Fig. 2c) along the zigzag direction, which shows the asymmetric behaviour in the $\theta = 0°$ and $180°$ directions (corresponding to positive and negative k-values, respectively). We will again focus on transitions from $p = 2$ to 9, which cover the same k-region, to isolate the diameter dependence of η. We show in Fig. 4a such $E_p(\mathbf{k})$ slices for transitions $p = 2$ (orange curve) and $p = 9$ (blue curve). In addition to a lower overall Fermi velocity as described previously, transition $p = 2$ also exhibits markedly stronger asymmetry. The dependence of asymmetry parameter η on p (or equivalently on $\bar{d}$ in the top axis) is displayed in Fig. 4b (dots), and it is fitted empirically by $\eta(p) = (50 + 180/p^2)$ meV nm^2 (solid line). Two factors contributed to this p dependence of η: modulated π-electron hopping coefficients from strain and the hybridization of σ and π states from the curved surface[24]. The strain acts like a pseudo-magnetic field threading the nanotubes. Its effect can be calculated analytically[25] and causes an increase in η by $85/p^2$ meV nm^2, ∼45% of our experimentally observed values in the wave-vector range $1.2 < k < 1.8$ nm^{-1}. The rest of the change in η probably

originates from σ–π bond hybridization. The effects of this magnitude are consistent with theoretical studies using a local density functional method[26].

In conclusion, we have compiled an atlas that allows us to identify the chiral index of a nanotube from a measurement of its optical resonances, and vice versa. In addition to providing a solid foundation for the spectroscopic identification of pristine nanotubes, this atlas allowed us to perform an in-depth study of many-body effects in a wide range of nanotubes, thus opening the way to further systematic investigations of this type.

Methods

Suspended long nanotubes were grown by chemical vapour deposition (CVD) across open slit structures (∼30 × 500 µm) fabricated on silicon substrates. We used methane in hydrogen (CH$_4$:H$_2$ = 1:2) as gas feedstock and a thin film (∼0.2 nm) of iron as the catalyst for CVD growth at 900 °C (ref. 27). This growth condition yields extremely clean isolated nanotubes free of amorphous carbon and other adsorbates (Supplementary Fig. S1)[28]. We determined the chiral index (n,m) of every nanotube from the electron diffraction pattern using nanofocused 80 keV electron beams in a JEOL 2100 transmission electron microscope (TEM)[29,30]. By utilizing the slit edges as spatial markers (Supplementary Fig. S1a), the same individual nanotubes can be identified in an optical microscope set-up. We probed optical transitions of these suspended nanotubes by Rayleigh scattering spectroscopy with a fibre-laser based supercontinuum light source covering the spectral range from 450 to 900 nm. The instrumental resolution in determining the transition energies was 5 meV.

References

1. Voit, J. One-dimensional Fermi liquids. *Rep. Prog. Phys.* **58,** 977–1116 (1995).
2. Bockrath, M. *et al.* Luttinger-liquid behaviour in carbon nanotubes. *Nature* **397,** 598–601 (1999).
3. Odom, T. W., Huang, J. L., Cheung, C. L. & Lieber, C. M. Magnetic clusters on single-walled carbon nanotubes: the Kondo effect in a one-dimensional host. *Science* **290,** 1549–1552 (2000).
4. Wang, F., Dukovic, G., Brus, L. E. & Heinz, T. F. The optical resonances in carbon nanotubes arise from excitons. *Science* **308,** 838–841 (2005).
5. Saito, R., Dresselhaus, G. & Dresselhaus, M. S. *Physical Properties of Carbon Nanotubes* (Imperial College Press, 1998).
6. Reich, S., Thomsen, C. & Maultzsch, J. *Carbon Nanotubes: Basic Concepts and Physical Properties* (Wiley, 2004).
7. Sfeir, M. Y. *et al.* Probing electronic transitions in individual carbon nanotubes by Rayleigh scattering. *Science* **306,** 1540–1543 (2004).
8. Sfeir, M. Y. *et al.* Optical spectroscopy of individual single-walled carbon nanotubes of defined chiral structure. *Science* **312,** 554–556 (2006).
9. Ando, T. Excitons in carbon nanotubes. *J. Phys. Soc. Jpn* **66,** 1066–1073 (1997).
10. Kane, C. L. & Mele, E. J. Ratio problem in single carbon nanotube fluorescence spectroscopy. *Phys. Rev. Lett.* **90,** 207401 (2003).

11. Kane, C. L. & Mele, E. J. Electron interactions and scaling relations for optical excitations in carbon nanotubes. *Phys. Rev. Lett.* **93,** 197402 (2004).
12. Perebeinos, V., Tersoff, J. & Avouris, P. Scaling of excitons in carbon nanotubes. *Phys. Rev. Lett.* **92,** 257402 (2004).
13. Spataru, C. D., Ismail-Beigi, S., Benedict, L. X. & Louie, S. G. Excitonic effects and optical spectra of single-walled carbon nanotubes. *Phys. Rev. Lett.* **92,** 077402 (2004).
14. Chang, E., Bussi, G., Ruini, A. & Molinari, E. Excitons in carbon nanotubes: an *ab initio* symmetry-based approach. *Phys. Rev. Lett.* **92,** 196401 (2004).
15. Zhao, H. B. & Mazumdar, S. Electron–electron interaction effects on the optical excitations of semiconducting single-walled carbon nanotubes. *Phys. Rev. Lett.* **93,** 157402 (2004).
16. Wang, F. *et al.* Observation of excitons in one-dimensional metallic single-walled carbon nanotubes. *Phys. Rev. Lett.* **99,** 227401 (2007).
17. Bachilo, S. M. *et al.* Structure-assigned optical spectra of single-walled carbon nanotubes. *Science* **298,** 2361–2366 (2002).
18. Lefebvre, J., Fraser, J. M., Homma, Y. & Finnie, P. Photoluminescence from single-walled carbon nanotubes: a comparison between suspended and micelle-encapsulated nanotubes. *Appl. Phys. A* **78,** 1107–1110 (2004).
19. Fantini, C. *et al.* Optical transition energies for carbon nanotubes from resonant Raman spectroscopy: environment and temperature effects. *Phys. Rev. Lett.* **93,** 147406 (2004).
20. Telg, H. *et al.* Chirality distribution and transition energies of carbon nanotubes. *Phys. Rev. Lett.* **93,** 177401 (2004).
21. Araujo, P. T. *et al.* Third and fourth optical transitions in semiconducting carbon nanotubes. *Phys. Rev. Lett.* **98,** 067401 (2007).
22. Novoselov, K. S. *et al.* Two-dimensional gas of massless Dirac fermions in graphene. *Nature* **438,** 197–200 (2005).
23. Zhang, Y. B., Tan, Y. W., Stormer, H. L. & Kim, P. Experimental observation of the quantum Hall effect and Berry's phase in graphene. *Nature* **438,** 201–204 (2005).
24. Blase, X., Benedict, L. X., Shirley, E. L. & Louie, S. G. Hybridization effects and metallicity in small radius carbon nanotubes. *Phys. Rev. Lett.* **72,** 1878–1881 (1994).
25. Kane, C. L. & Mele, E. J. Size, shape, and low energy electronic structure of carbon nanotubes. *Phys. Rev. Lett.* **78,** 1932–1935 (1997).
26. Reich, S., Thomsen, C. & Ordejon, P. Electronic band structure of isolated and bundled carbon nanotubes. *Phys. Rev. B* **65,** 155411 (2002).
27. Huang, S. M., Cai, X. Y. & Liu, J. Growth of millimeter-long and horizontally aligned single-walled carbon nanotubes on flat substrates. *J. Am. Chem. Soc.* **125,** 5636–5637 (2003).
28. Liu, K. H. *et al.* Intrinsic radial breathing oscillation in suspended single-walled carbon nanotubes. *Phys. Rev. B* **83,** 113404 (2011).
29. Liu, Z. J. & Qin, L-C. A direct method to determine the chiral indices of carbon nanotubes. *Chem. Phys. Lett.* **408,** 75–79 (2005).
30. Liu, K. H. *et al.* Direct determination of atomic structure of large-indexed carbon nanotubes by electron diffraction: application to double-walled nanotubes. *J. Phys. D* **42,** 125412 (2009).

Author contributions

F.W., E.W. and K.L. conceived the experiment. K.L., F.X., X.H. and F.W. carried out the optical measurements. K.L., S.A. and X.B. carried out structural characterization. K.L., W.W. and A.Z. contributed to growing the sample. J.D., R.B.C., S.G.L. and F.W. performed theoretical analysis. All authors discussed the results and wrote the paper.

Additional information

The authors declare no competing financial interests. Supplementary information accompanies this paper at www.nature.com/naturenanotechnology. Reprints and permission information is available online at http://www.nature.com/reprints. Correspondence and requests for materials should be addressed to F.W. or E.W.